EARTH SURFACE PROCESSES AND LANDFORMS
Earth Surf. Process. Landforms (2017)

Published online in Wiley Online Library
(wileyonlinelibrary.com) DOI: 10.1002/esp.4260

Does the permeability of gravel river beds affect near-bed hydrodynamics?

James R. Cooper,[1]* Annie Ockleford,[2] Stephen P. Rice[3] and D. Mark Powell[4]
[1] Department of Geography and Planning, School of Environmental Sciences, University of Liverpool, Liverpool L69 7ZT, UK
[2] School of Environment and Technology, University of Brighton, Brighton BN2 4GJ, UK
[3] Centre for Hydrological and Ecosystem Science, Department of Geography, Loughborough University, Loughborough LE11 3TU, UK
[4] Department of Geography, University of Leicester, Leicester LE1 7RH, UK

Received 10 May 2017; Revised 31 August 2017; Accepted 11 September 2017

*Correspondence to: James Cooper, School of Environmental Sciences, Roxby Building, University of Liverpool, Liverpool, L69 7ZT, UK. E-mail: james.cooper@liverpool.ac.uk

ESPL
Earth Surface Processes and Landforms

ABSTRACT: The permeability of river beds is an important control on hyporheic flow and the movement of fine sediment and solutes into and out of the bed. However, relatively little is known about the effect of bed permeability on overlying near-bed flow dynamics, and thus on fluid advection at the sediment–water interface. This study provides the first quantification of this effect for water-worked gravel beds. Laboratory experiments in a recirculating flume revealed that flows over permeable beds exhibit fundamental differences compared with flows over impermeable beds of the same topography. The turbulence over permeable beds is less intense, more organised and more efficient at momentum transfer because eddies are more coherent. Furthermore, turbulent kinetic energy is lower, meaning that less energy is extracted from the mean flow by this turbulence. Consequently, the double-averaged velocity is higher and the bulk flow resistance is lower over permeable beds, and there is a difference in how momentum is conveyed from the overlying flow to the bed surface. The main implications of these results are three-fold. First, local pressure gradients, and therefore rates of material transport, across the sediment–water interface are likely to differ between impermeable and permeable beds. Second, near-bed and hyporheic flows are unlikely to be adequately predicted by numerical models that represent the bed as an impermeable boundary. Third, more sophisticated flow resistance models are required for coarse-grained rivers that consider not only the bed surface but also the underlying permeable structure. Overall, our results suggest that the effects of bed permeability have critical implications for hyporheic exchange, fluvial sediment dynamics and benthic habitat availability. Copyright © 2017 John Wiley & Sons, Ltd.

KEYWORDS: bed permeability; hydrodynamics; gravel bed; flume; river

Introduction

The permeability of river beds is an important control on hyporheic flow (Sawyer and Cardenas, 2009) and the movement of fine sediment (Chen *et al*., 2010) and solutes (Marion *et al*., 2008) into and out of the bed. However, relatively little is known about the effect of bed permeability on overlying near-bed hydrodynamics, despite interfacial transport usually being driven by pore water advection caused by turbulent coupling with the overlying flow (Packman and Bencala, 2000; Cardenas and Wilson, 2007). We are aware of only one study that has examined this effect within the context of river beds. Blois *et al*. (2014) examined the flow over a coarse-grained 2-D dune and revealed key differences depending on whether the dune sat on an impermeable or permeable bed (composed of cubically packed spheres). Using flume experiments they found the reattachment region to either move further downstream or to be absent on a permeable bed, plus the area of upwelling over the dune was larger, and the shear layer had a lower Reynolds stress. Sinha *et al*. (2017) examined these differences further by producing numerical simulations of these experiments. Their simulations revealed the size of the recirculation zone in the leeside of a dune was smaller over a permeable bed because of jets of flow leaving the hyporheic zone and entering the overlying flow. These jets resulted in the turbulent kinetic energy being much lower in the lee than observed over an impermeable bed. However coarse-grained fluvial deposits rarely have such a simple, regular geometry as examined by Blois *et al*. (2014) and Sinha *et al*. (2017). During sediment transport, heterogeneous particle sizes, shapes and angularity promote the development of complex bed structures comprising particle imbrication, clustering and other complex packing arrangements which have important consequences for permeability (Cooper and Tait, 2009; Haynes *et al*., 2012). Thus, the pores that connect the overlying flow with the subsurface flow have a range of sizes, geometries and orientations, which are likely to have a different effect on the near-bed flow than a deposit with a simple, regular geometry. Therefore, to understand the effect of the permeability of coarse-grained fluvial deposits on sediment–water exchange

processes, a detailed investigation of its effect on near-bed flow dynamics is required.

Over permeable beds significant exchanges of mass and momentum occur across the sediment–water interface due to pressure gradients that drive flow into and out of the bed (Elliott and Brooks, 1997; Huettel and Webster, 2001; Cardenas and Wilson, 2007; Boano *et al.*, 2014). These pressure gradients contain two components: (i) a steady, hydrostatic component related to variations in the depth of the flow that are typically induced by larger, emergent topographic features, such as riffles and pools (Harvey and Bencala, 1993; Tonina and Buffington, 2007); and (ii) a local, fluctuating component caused by turbulent coupling between the overlying and pore water that drives shallow interfacial exchange, often termed turbulent pumping or hydrodynamic forcing (Boano *et al.*, 2014). This coupling occurs because flow is hydrodynamically forced into the pores by coherent turbulent vortices that generate significant velocity and pressure fluctuations across the bed and in the pores beneath (Nagaoka and Ohgaki, 1990; Packman and Bencala, 2000; Huettel and Webster, 2001; Detert *et al.*, 2004; 2010a; 2010b). However because no sediment–water exchange can occur over an impermeable bed, and a no-slip condition applies at the solid surface, one would expect local pressure gradients, and thus the mean and turbulent characteristics of the overlying flow, to differ from that of a permeable bed. The lack of turbulent coupling, in particular, is likely to impact upon the generation and size of coherent eddies, and therefore their role in momentum transfer and pumping water into and out of the bed (Nagaoka and Ohgaki, 1990; Boano *et al.*, 2011). For example, over an impermeable bed there is no subsurface flow to promote the production of ejections transferring fluid from the surface grains to the overlying flow, and when a sweep coming from above interacts with the solid surface its vertical motions are impeded and the energy is transferred downwards with almost zero vertical velocity (Blois *et al.*, 2014). Thus coherent motions over impermeable beds may be less important in the production of turbulent kinetic energy, and overall turbulence may contribute less to momentum transfer. However a detailed quantification of these differences in the near-bed hydrodynamics over coarse-grained permeable and impermeable beds is lacking.

Such understanding is needed for a number of important reasons. First, river flow models that predict velocity distributions across the sediment–water interface, including those that drive the modelling of hyporheic flow (Cardenas and Wilson, 2007; Qian *et al.*, 2008; Zhou *et al.*, 2014), commonly assume the bed surface is impermeable (Keylock *et al.*, 2012). A difference in near-bed hydrodynamics between permeable and impermeable beds would suggest these models may yield unrealistic predictions of local pressure gradients. For example, numerical simulations by Boano *et al.* (2011) suggest that an inaccurate representation of the fluctuating pressure gradients resulting from coherent motions would have critical implications for prediction of the depth and velocity at which water pumps into and out of fluvial deposits, and thus the mixing between surface water and groundwater. Second, estimates of flow resistance parameters, such as the Manning coefficient or equivalent sand roughness height, are commonly related to a characteristic bed grain diameter (Hey, 1979; Bathurst, 1985; Bray, 1985; Wiberg and Smith, 1991) or the standard deviation of bed elevations (Aberle and Smart, 2003; Coleman *et al.*, 2011). These measures are the same for permeable and impermeable beds that have the same surface topography, so permeable and impermeable beds yield the same estimates of flow resistance. Thus applying a flow resistance parameter without accounting for both the surface layer of grains and bed permeability may provide inaccurate estimates of water velocity and depth, and ultimately flooding area extent and severity. Third, interfacial transport is normally driven by turbulent coupling between the overlying and pore water flow (Packman and Bencala, 2000; Cardenas and Wilson, 2007). Therefore a new quantification of the effect of permeability, and associated surface–subsurface flow coupling, on near-bed hydrodynamics would be beneficial for improving models of contaminant and fine sediment ingress and storage (Packman *et al.*, 2000; Bencala *et al.*, 2011), biogeochemical processing in the hyporheic zone (Battin *et al.*, 2008; Mulholland *et al.*, 2008; Palumbo-Roe *et al.*, 2012), and the spawning habitat of some fish (Boulton *et al.*, 1998; Suttle *et al.*, 2004).

This paper addresses the fundamental question of whether the near-bed hydrodynamics over coarse-grained permeable beds is significantly different from impermeable beds. We present a series of flume experiments that examined near-bed hydrodynamics over complex, water-worked permeable gravel beds and also over replica versions of those beds that were impermeable but had the same surface topography. The experiments form the basis for evaluating the link between bed permeability and flow dynamics, thereby overcoming a major flaw in current understanding of interfacial exchange processes. The collected data is used to explore the impact of bed permeability on the mean and turbulent flow components, bursting events associated with coherent eddies, and the size and importance of these eddies in fluid momentum transfer and the production of turbulent kinetic energy. This research offers the first insight into the significance of bed permeability for governing momentum exchange at the sediment–water boundary of coarse-grained river beds. In so doing, we highlight that the effects of bed permeability have critical implications for hyporheic exchange, fluvial sediment dynamics and benthic habitat availability.

Methodology

Overview

The paper presents results comparing three permeable sediment beds with their impermeable facsimiles. Experiments were performed within a rectangular, glass sided recirculating flume (8.2 m × 0.6 m × 0.5 m). The permeable beds were created using different bedload transport rates. A casting technique developed by Buffin-Bélanger *et al.* (2003) was then used to produce impermeable facsimiles of each of the permeable beds that replicated faithfully the topography of the original surfaces. This allowed the effects of permeability on the near-bed hydrodynamics to be isolated from other effects such as those caused by differences in surface microtopography. The near-bed flow over these beds was measured using Particle Image Velocimetry (PIV) and used to examine the temporal and spatial dynamics of the near-bed flow.

Experimental surfaces

The three beds were created using one well-sorted grain size distribution (sorting = 1.5 (Folk and Ward, 1957); 1 mm $< D <$ 45 mm; D_{50} = 8 mm; D_{84} = 23 mm) of natural fluvial sands and gravels. Each bed was produced by water-working the mixture at different initial transport rates (Table I). The size distribution of the sediment was not scaled directly from field samples, however, the sorting value is representative of the lower limit of values of 148 subsurface grain-size distributions from nine gravel-bed rivers, in Canada, USA, France,

Table I. Properties of the experimental bed surfaces, where S is the flume slope used to water-work the surface, D_x is the xth percentiles of the bed surface grain size distribution, σ_s is the sorting coefficient for the bed surface (calculated according to Folk and Ward, 1957), i_b is sediment transport rate, σ_z is the standard deviation in bed surface elevations, and k is the range in elevations (= $z_{99} - z_{01}$, where z_{xx} is the level at which xx% of observed bed elevations are smaller), and τ^* is the dimensionless bed shear stress at the start of water-working, calculated as $\tau^* = \tau/(\rho_s - \rho)gD_{50}$, where $\tau = \rho gRS$ (corrected for sidewall effects using the method of Williams, 1970), ρ_s is sediment density, ρ is water density, and g is acceleration due to gravity, R is hydraulic radius

		Initial parameters[a]				Final parameters[b]			
Bed	S [−]	D_{50} (D_{84}) [mm]	σ_s [−]	τ^* [−]	i_b [g m^{-1} s^{-1}]	D_{50} (D_{84}) [mm]	σ_s [−]	σ_z [mm]	k [mm]
A	0.006	9.9 (19.7)	1.1	0.031	24.0	12.5 (22.5)	1.0	8.0	38.8
B	0.006	9.0 (20.8)	1.2	0.034	16.1	13.5 (25.4)	0.9	5.4	26.1
C	0.009	9.4 (19.2)	1.1	0.049	51.5	16.1 (26.5)	0.9	9.4	36.1

[a]Measured at $t = 0$ min except the initial transport rate which is sampled at $t = 10$ min.
[b]Measured at $t = 1200$ min.

New Zealand and UK. These distributions were collected by the authors or provided by colleagues (see acknowledgments). For each bed, the flume slope was set to either $S = 0.006$ or 0.009 (Table I) and the bed screeded to a depth of 90 mm (an equivalent depth of $\sim 11 D_{50}$), so the sediment surface was parallel to the flume floor. Pressure fluctuations due to overlying turbulent flow penetrate to a depth of $z/k_s \approx -3$ in the subsurface of gravels (Detert *et al.*, 2010b), where z is the height above the bed and k_s is the equivalent sand-grain roughness height. This threshold equates to depths of 36–61 mm below the surface for the studied flow conditions. Thus a bed depth of 90 mm was sufficient to allow the affect of bed permeability to be studied. A consolidation phase was then run for 30 min over the screeded bed at 10 mm flow depth. Flow was then increased to a depth h of 120 mm and used to water-work the surface for 1200 min. The relative roughness (h/D_{84}) of the experimental mixture was 5.2 and, therefore, at the lower end of values that are typically observed in gravel-bed rivers ($h/D_{84} > 5$; Bathurst, 1993). During this phase of water-working, sediment was recirculated whereby sediment collected in a sediment trap at the downstream end of the flume was re-entered at the upstream end. For the first 60 min of each experiment, transport rates were high due to the unconsolidated nature of the bed. Sediment was therefore recirculated more frequently during these early stages of the experiments. Sediment was recirculated every 10 min for the first half an hour, every 15 min during the following half an hour and thereafter at $t = 120$, 180, 360, 620 and 900 min. The recirculation formed a mobile armour layer, when the sediment transport rate no longer fluctuated significantly. The water-worked surfaces obtained at $t = 1200$ were therefore adjusted to equilibrium transport rates, each developing a small bed slope relative to the flume floor. The downstream adjustable weir was laid flat throughout the water-working phase to allow the flow depth to adjust naturally. The bed was re-mixed and screeded between experiments to avoid inheritance effects.

A rigid steel tray (1000 × 400 mm), with its upstream edge 3 m from the flume inlet, was placed on the flume floor and buried with the test sediments during screeding. The tray allowed removal of a portion of the bed to facilitate measurements of surface topography, which were made outside the flume. The topography of the central 400 × 400 mm of the tray (the test section) was captured using a hand-held laser scanner (Faro Laser Line Probe®) mounted on a seven-axis articulated arm (Faro ScanArm®). The three beds provide examples for testing whether the effect of bed permeability on near-bed hydrodynamics is consistent. Figure 1 shows that each bed has a different microtopography but all are grain-roughness dominated and have the typical particle imbrication and clustering found on water-worked surfaces (Marion *et al.*, 2003; Cooper and Tait, 2009; Hodge *et al.*, 2009; Bertin and Friedrich, 2014). Bed C is slightly coarser ($D_{50} = 12.5$, 13.5 and 16.1 mm for beds A, B and C, respectively) with more variation in surface elevation than A and B ($\sigma_z = 8.0$, 5.4 and 9.4 mm on beds A, B and C, respectively; Table I). Across all three beds the difference in elevation standard deviation and D_{84} is just 4 mm.

Bed casting

The impermeable facsimiles were made of the test section after the scanning had taken place, using the casting technique described in Buffin-Bélanger *et al.* (2003) so only a brief description is given here. A wooden retaining frame was placed over the test section and a mould was made of the surface contained within it. This was achieved using a polyvinyl chloride, Gelflex™, which was melted and poured over the

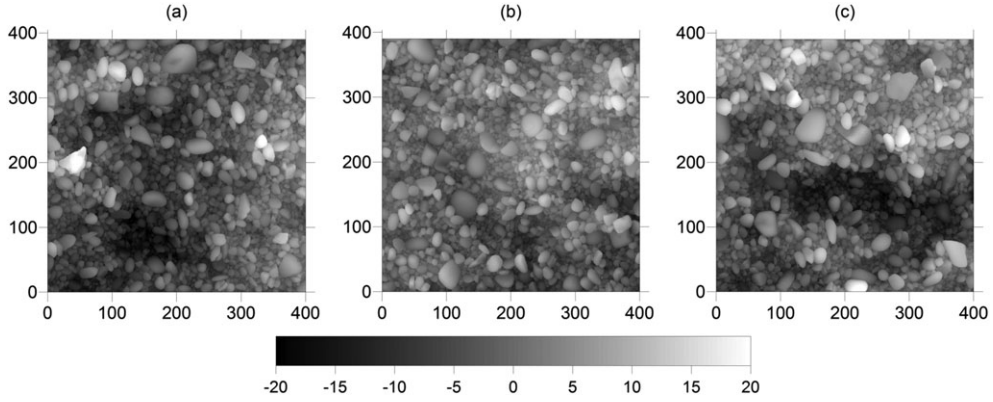

Figure 1. DEMs of (a) Bed A, (b) Bed B and (c) Bed C. The flow is from left to right and the axes dimensions are in mm. The greyscale relates to the departure in elevation from the zero mean surface elevation (mm).

sediment surface. In order to create rigidity and maintain the integrity of this moulded surface, a polyurethane foam resin, which expands and cures to become inflexible, was sprayed onto the solidified layer of Gelflex™. When the foam had set, the wooden retaining frame was removed, turned upside down and any sediment which was stuck to the Gelflex™ removed to leave a negative impression of the gravel surface, including the upper portions of deep and complex interstices (Figure 2). A mould was subsequently made to replicate the original surface in the form of an impermeable cast. The mould was created using a mixture of epoxy and polyurethane resins. The final step was the removal of the foam and Gelflex™ from the resin surface to reveal an impermeable facsimile of the original permeable surface.

A test of the performance of the casting technique in producing accurate impermeable facsimiles was reported in Buffin-Bélanger *et al.* (2003). Photogrammetric surveys were undertaken both before and after the surface was replicated and a DEM of difference taken of the original and cast surface. Their results revealed maximum differences of ±3 mm or 0.08 D_{50} with the only notable differences being observed in areas defined by large particles. Note that the median particle size used in the current experiments is approximately four times smaller than used by Buffin-Bélanger *et al.* (2003).

Since the casts were made over a period of several months in line with a wider experimental programme, other tests took place between the flow measurements being made over the permeable bed and over the cast. Thus the surrounding sediment bed was not the same as the one used to create the cast surface. Instead a sediment bed of the same mixture was again water-worked using the same conditions as was used to form the permeable bed. Consequently the casts were tested in a flow that was conditioned by the same bed and hydraulic properties, and although the exact microtopography upstream was different, the general flow properties were similar. The impermeable bed casts were carefully placed in the flume, ensuring there was no physical disturbance to neighbouring grains. The flow was then set to the same conditions as were used for the PIV measurements over the permeable beds and flow measurements taken at the same location.

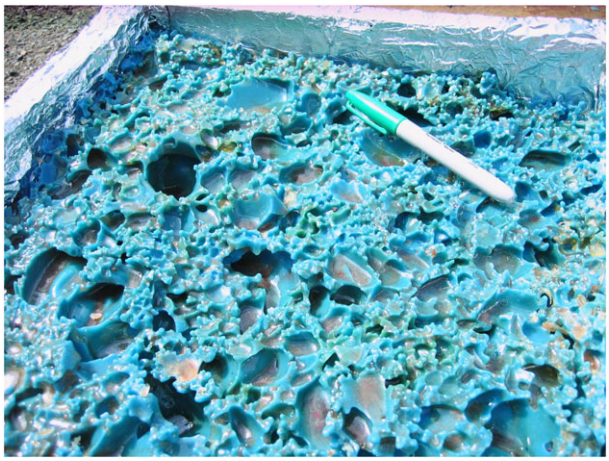

Figure 2. A Gelflex™ mould revealing a fascinating negative impression of the gravel surface with variably deep and complex interstices. [Colour figure can be viewed at wileyonlinelibrary.com]

Velocity measurements

Velocity measurements of the near-bed flow were taken over the final bed surfaces and their impermeable facsimiles using a Dantec 2D, double-pulsed Nd:YAG laser, Particle Image Velocimetry (PIV) system. To ensure bed material did not move during the flow measurements, the flume slope was dropped so the bed slope of the final surface was equal to the initial slope used to water-work the beds (0.006 for beds A and B, and 0.009 for bed C). For each surface, a steady, fully turbulent flow with a uniform depth of 120 mm was generated within the flume by adjusting the discharge (Table II), ensuring the relative submergence was the same, which is important when comparing near-bed hydrodynamics (Cooper *et al.*, 2013). The flow was sampled for 60 s (cf. Buffin-Bélanger and Roy, 2005) at a frequency of 20 Hz. The light sheet was aligned along the flume centreline, the centreline of the test section (for both the original permeable bed and impermeable facsimile), normal to the bed surface and parallel to the flume walls. This configuration enabled streamwise and vertical velocities to be measured. An area of 300 × 240 mm was imaged, with the longer axis in the streamwise direction. The PIV image interrogation areas were overlapped in the streamwise and lateral direction by 50%, increasing the probability that seeding particles close to the edges of each area contributed to the velocity estimation. This processing produced 76 vectors in the streamwise direction and up to 63 vectors in the vertical direction, resulting in a total of 4788 measurements within each image with a separation distance of 3.94 mm and 3.80 mm between each velocity vector (in streamwise and vertical directions, respectively).

Spatially-averaged flow analysis

To determine the overall effect of bed permeability on the time-averaged and turbulent components of the flow, we examined spatially-averaged (or double-averaged) flow properties (Nikora *et al.*, 2007). Spatial averaging was conducted along the streamwise length of the sampled flow area (300 mm) at each measurement height. We have used spatial averaging for two reasons. The first reason is a pragmatic one; the approach is a useful way to summarise spatially-rich flow data. The

Table II. Summary of the tested flow conditions, where S is bed slope, Q is flow discharge, h is flow depth, k is the range of bed surface elevations (= $z_{99} - z_{01}$), D_{84} is the 84th percentile of the bed surface grain size distribution, u_* is shear velocity, U is depth-averaged velocity and Re is the bulk Reynolds number calculated as $\mathrm{Re} = \rho UR/\mu$, ρ is density of water, R is hydraulic radius and μ is dynamic viscosity

Test	S [−]	Q [m^3 s^{-1}]	h [m]	h/k [−]	h/D_{84} [−]	u_* [m s^{-1}]	U [m s^{-1}]	Re [−]
Bed A: Permeable	0.006	0.051	0.12	3.1	5.3	0.071	0.85	68651
Bed A: Impermeable	0.006	0.047	0.12	3.1	5.3	0.069	0.79	63805
Bed B: Permeable	0.006	0.050	0.12	4.6	4.7	0.068	0.84	67843
Bed B: Impermeable	0.006	0.048	0.12	4.6	4.7	0.064	0.80	64612
Bed C: Permeable	0.009	0.062	0.12	3.3	4.5	0.084	1.04	83996
Bed C: Impermeable	0.009	0.059	0.12	3.3	4.5	0.082	0.98	79150

second, and more pertinent reason, is the approach enables us to analyse better the complex behaviour of flow over rough microtopography (Finnigan and Shaw, 2008). In the study of turbulent flows the convention is to use temporal averaging to separate the random part of the flow from the slowly varying or 'mean' component. This single averaging process is useful for identifying how the two components interact e.g. how turbulent eddies obtain energy from the mean flow. In ideal flows (incompressible, inviscid flows), this separation is straightforward and unambiguous, because the turbulence is statistically homogeneous in time and space, but in gravel-bed flows it is not. This difficulty arises because the turbulent part of these viscous flows is not completely random. Over gravel surfaces the flow must find its way around the grains so a spatial variability is forced directly upon the flow field. Thus the flow contains structures that are coherent in time and space. Although these eddies are located randomly in time or space, they have a reproducible spatial pattern and are sufficiently regular to be less random than the more incoherent background turbulence. Thus, these persistent vortices are separate from the background turbulence and contribute to the total flux of momentum. Time-averaging is therefore not sufficient because the flow behaviour is more complex than can be explained by a simple partition into random and mean components. Additional spatial averaging is required to estimate the additional momentum transferred towards the surface grains by these persistent vortices (Cooper and Tait, 2010). This additional momentum is known as form-induced stress.

The following spatially-averaged flow parameters were examined: (i) double-averaged streamwise velocity $\langle\overline{u}\rangle$ where $\overline{u}$ is the time-averaged velocity and angled brackets denote spatially-averaged; (ii) spatially-averaged streamwise and lvertical turbulence intensity $\left\langle\overline{u'^2}\right\rangle^{0.5}$ and $\left\langle\overline{w'^2}\right\rangle^{0.5}$, where $u' = u - \overline{u}$, $w' = w - \overline{w}$, u and w are instantaneous streamwise and vertical velocities and $\overline{u}$ and $\overline{w}$ are the time-averaged velocities; (iii) spatially-averaged Reynolds stress $\left\langle\overline{u'w'}\right\rangle$; (iv) turbulence correlation coefficient $r_R = -\left\langle\overline{u'w'}\right\rangle / \left(\left\langle\overline{u'^2}\right\rangle\left\langle\overline{w'^2}\right\rangle\right)^{0.5}$; (v) spatially-averaged turbulent kinetic energy $K = 0.5\left\langle\overline{u'^2} + \overline{w'^2}\right\rangle$; (vi) spatial fluctuations in streamwise and vertical velocity $\left\langle\widetilde{u}^2\right\rangle^{0.5}$ and $\left\langle\widetilde{w}^2\right\rangle^{0.5}$, termed the streamwise and vertical form-induced intensity, where the spatial fluctuations result from the difference between the double-averaged and time-averaged values, $\widetilde{u} = \overline{u} - \langle\overline{u}\rangle$ and $\widetilde{w} = \overline{w} - \langle\overline{w}\rangle$; (vii) form-induced stress $\langle\widetilde{u}\widetilde{w}\rangle$ that arises due to correlations in the spatial fluctuations in time-averaged velocity (these correlations can exist as the flow field as it finds its way around the grains on the bed surface, and can contribute to the total flux of momentum); and (viii) form-induced correlation coefficient $r_F = \mathrm{I}\langle\widetilde{u}\widetilde{w}\rangle\mathrm{I} / \left(\left\langle\widetilde{u}^2\right\rangle\left\langle\widetilde{w}^2\right\rangle\right)^{0.5}$. The shear velocity u_* was determined by fitting the double-averaged velocity profile above the roughness crest with the following logarithmic law, using a Clauser-type analysis:

$$\langle\overline{u}\rangle = \frac{u_*}{\kappa}\ln\left(\frac{z-d}{z_0}\right) \tag{1}$$

where κ is the von Karman constant (set to 0.41), z_0 is the roughness height, and d is the displacement height. This approach was chosen because it does not require *a priori* definition of the zero-displacement plane.

Quadrant analysis

Quadrant analysis was used to investigate bursting events produced by coherent eddies. The technique is based on the analysis of the joint distribution of the velocity fluctuations u' and w' from the time-averaged streamwise and vertical velocity to detect the type of event (Lu and Willmarth, 1973). A detecting function $\lambda_{i;H}(t)$ is used to determine if the (u', w') pair is larger than a hole size H: $\lambda_{i;H}(t) = 1$ if the (u', w') pair is in quadrant i and if $u'w' \geq H\overline{u'w'}$, and $\lambda_{i;H}(t) = 0$ if $u'w' < H\overline{u'w'}$. The proportion of time spent in each quadrant $T_{i;H}$ is given by

$$T_{i,H} = \frac{1}{T}\int_0^T u'(t)w'(t)\lambda_{i,H}(z,t)dt \tag{2}$$

where T is the sampling time, and was spatially-averaged to give $\langle T_{i,H}\rangle$. The four quadrants i (= 1, 2, 3, and 4) correspond to four types of bursting events: outward interactions $Q1$ ($i=1$; $u'>0, w'>0$); ejections $Q2$ ($i=2$; $u'<0$, $w'>0$); inward interactions $Q3$ ($i=3$; $u'<0$, $w'<0$); and sweeps $Q4$ ($i=4$; $u'>0$, $w'<0$). The analysis was performed for three hole sizes ($H=0$, 1 and 2), leaving the weaker (u', w') pairs within the hole, to examine how the difference in $\langle T_{i,H}\rangle$ between the permeable and impermeable beds changed with the intensity of the quadrant events.

Two-point velocity correlation

To quantify the size of coherent eddies within the velocity fields, the two-point correlation coefficient R_{uw} between u' and w' was calculated:

$$R_{uw}(\Delta x, \Delta z) = \frac{\overline{u'(x,z)w'(x+\Delta x, z+\Delta z)}}{\overline{u'(x,z)w'(x,z)}} \tag{3}$$

where Δx and Δz are separations in the streamwise and vertical directions, respectively. The overline notation represents an ensemble average over multiple realisations.

Large eddies produce most of the Reynolds stress and turbulent kinetic energy (TKE) in gravel-bed flows (Mignot *et al.*, 2009). As a result, they dominate the two-point correlations (Moin and Moser, 1989), and their typical size can be estimated by the Eulerian length scale. This scale is equal to the separation in distance over which velocity fluctuations remain correlated.

Virtually all estimates of the Eulerian length scale obtained for gravel-bed flows are derived from correlations of single point time series at different temporal lags. The Taylor's frozen turbulence hypothesis is used to convert these lags to dimensions of streamwise length using the time-averaged velocity at the height of measurement (Roy *et al.*, 2004). This hypothesis is questionable however because large eddies occupy areas of considerably different mean velocity. The use of two-point velocity correlations has two advantages over this existing approach (Shaw *et al.*, 1995): (i) using different spatial lags, two-point correlations provide direct calculation of the length scale without the need to assume Taylor's hypothesis; and (ii) the correlations can also provide estimates of the typical eddy height. The streamwise and vertical length scales L_x and L_z are defined in the following manner:

$$L_x = \int_0^\infty R_{uw}(\Delta x, 0)d\Delta x \tag{4}$$

$$L_z = \int_0^{\infty} R_{uw}(0, \Delta z) d\Delta z \tag{5}$$

Proper orthogonal decomposition

Proper orthogonal decomposition (POD) was used to quantify the relative importance of coherent eddies in producing turbulent fluctuations. The POD technique is able to identify patterns of simultaneous fluctuation in velocity through a decomposition of the measured flow field using a set of orthogonal eigenfunctions and associated eigenvalues. The functions contain the spatial structure of the turbulent flow, and the sum of the eigenvalues is equal to the total TKE. Thus the set of eigenvalues represents the distribution of energy at different orthogonal eigenmodes. The rate at which these eigenvalues coverage is therefore a measure of both the presence and relative importance of eddies in producing TKE. It follows that in flows dominated by coherent motions a large fraction of the TKE is captured in just the first few modes, whereas in flows with no dominant structure there is a more even distribution of energy across the modes.

The first step in POD analysis is to calculate the autocorrelation matrix C of the total energy in the flow at every instance in time:

$$C(t_1, t_2) = \frac{1}{N} \iint \left(u'(x, z, t_1) u'(x, z, t_2) + w'(x, z, t_1) w'(x, z, t_2) \right) dx dz \tag{6}$$

where N is the number of vector fields. The eigenvalue problem $CA_i = \lambda_i A_i$, is then solved, where A is the matrix of eigenvectors of the C matrix, λ are its eigenvalues and i is the eigenmode number ($i = 1,..,N$). The solutions are ranked in a decreasing order according to the magnitude of the eigenvalues: $\lambda_1 > \lambda_2 > ... > \lambda_N$. The ith eigenvalue is a measure of the amount of TKE transferred within the corresponding ith eigenmode (Fukunaga, 1990). The ranking of the eigenvalues therefore reflects their importance in terms of transferring energy; as the mode increases the total mode energy, and the size and energy of eddies, decreases. Thus to quantify the role of dominant large eddies in producing TKE the first modes must be examined. The relative energy contained within each mode E is given by

$$E_i = \frac{\lambda_i}{\sum_{i=1}^{N} \lambda_i} \tag{7}$$

These relative energies are compared between the permeable and impermeable beds to examine whether the lack of turbulent streamwater–pore water coupling over the latter has an impact on the role of coherent eddies in the production of TKE.

Results

Spatially-averaged flow

The double-averaged streamwise velocity profiles in the near-bed region are presented in Figure 3(a). The dashed line denotes the roughness crest and thus the top of the interfacial sublayer (where $z - z_{max} = 0$; z is the measurement height and z_{max} is the roughness crest). The figure shows that for each of the three surfaces, flow velocity is higher over the permeable bed within the interfacial sublayer. Higher up in the flow, the velocity is higher over the permeable beds of A and C. These differences are summarised at the roughness crest in Table III and in Figure 4(a). The roughness crest is chosen because it is the height at which there is maximum fluid exchange at the sediment–water interface (Mignot *et al.*, 2009). Taking Bed B as an example, the normalised velocity $\langle \overline{u} \rangle / u_*$ at the roughness crest is 8.09 over the permeable bed but is just 6.73 over the impermeable bed. Overall, at the roughness crest the velocity ranges from being 5–20% higher over the permeable beds (Figure 4(a)).

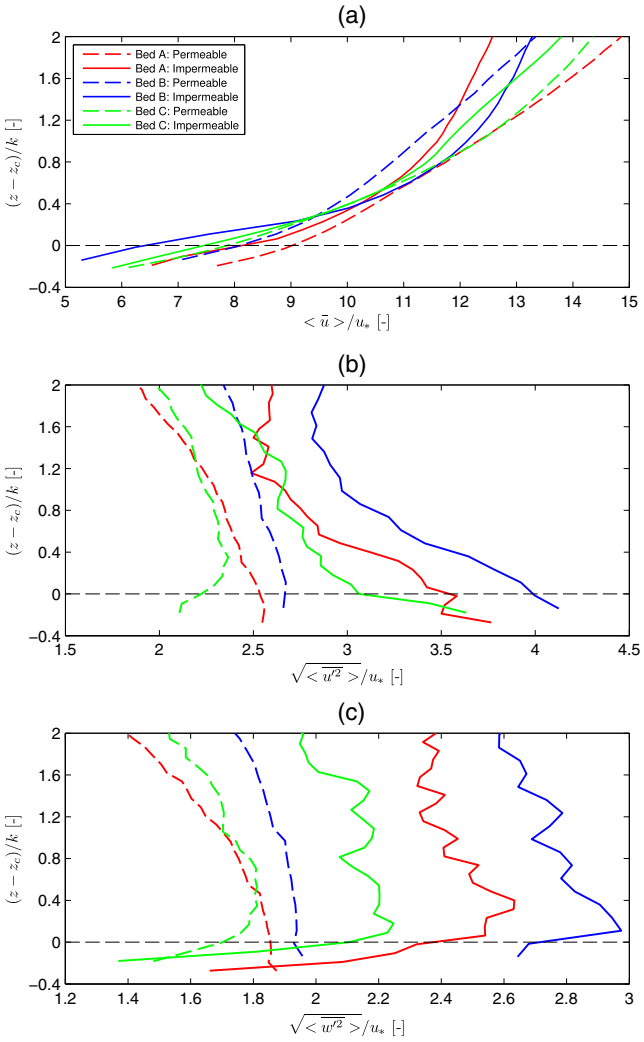

Figure 3. Vertical profiles of (a) double-averaged velocity; (b) streamwise turbulence intensity; and (c) vertical turbulence intensity, where z is the measurement height, z_c is the roughness crest (= z_{99}) and k is the range of bed elevations. The dashed line denotes the top of the interfacial sublayer and the roughness crest. [Colour figure can be viewed at wileyonlinelibrary.com]

The turbulence intensities are lower over the permeable beds (Figure 3(b), (c)). At the roughness crest, the streamwise turbulence intensity is lower by a similar degree over the three beds (28%, 33% and 27% for the streamwise turbulence intensity, and 22%, 29% and 19% for the vertical turbulence intensity, for beds A, B and C, respectively; Figure 4(b), (c)). However, despite these lower intensities the momentum flux at the roughness crest arising from these temporal fluctuations, the Reynolds stress, is higher over the permeable bed (Table III). The stress is 34%, 12% and 10% higher over beds A, B and C, respectively (Figure 4(d)). The turbulence correlation coefficients reveal this higher momentum flux occurs because the turbulent flow is more coherent in the temporal domain (Table III). For example, for Bed B the coefficient is 0.2 over the permeable bed but only 0.06 over the impermeable bed. Although the Reynolds stress and coefficients are higher, the

Table III. Flow statistics at the roughness crest

	Bed A		Bed B		Bed C	
Parameter	**Permeable**	**Impermeable**	**Permeable**	**Impermeable**	**Permeable**	**Impermeable**
$\langle\overline{u}\rangle/u_*$ [−]	9.02	8.13	8.09	6.73	7.86	7.46
$\left\langle\overline{u'^2}\right\rangle^{0.5}/u_*$[−]	2.54	3.54	2.67	3.99	2.22	3.06
$\left\langle\overline{w'^2}\right\rangle^{0.5}/u_*$[−]	1.85	2.38	1.93	2.72	1.70	2.11
$\left\langle\overline{u'w'}\right\rangle/u_*^2$[−]	1.03	0.77	1.02	0.91	0.69	0.63
r_R [−]	0.22	0.078	0.20	0.056	0.18	0.15
$K^{0.5}/u_*$ [−]	2.23	3.05	2.33	3.52	1.97	2.73
$\left\langle\widetilde{u}^2\right\rangle^{0.5}/u_*$ [−]	0.31	0.67	0.35	1.49	0.88	1.20
$\left\langle\widetilde{w}^2\right\rangle^{0.5}/u_*$ [−]	0.31	0.47	0.42	0.57	0.60	0.65
$\lvert\langle\widetilde{u}\widetilde{w}\rangle\rvert/u_*^2$ [−]	0.02	0.17	0.08	0.43	0.13	0.37
r_F [−]	0.22	0.50	0.51	0.56	0.25	0.47
L_x/h [−]	0.39	0.55	0.37	0.41	0.35	0.51
L_z/h [−]	0.16	0.18	0.15	0.17	0.16	0.16

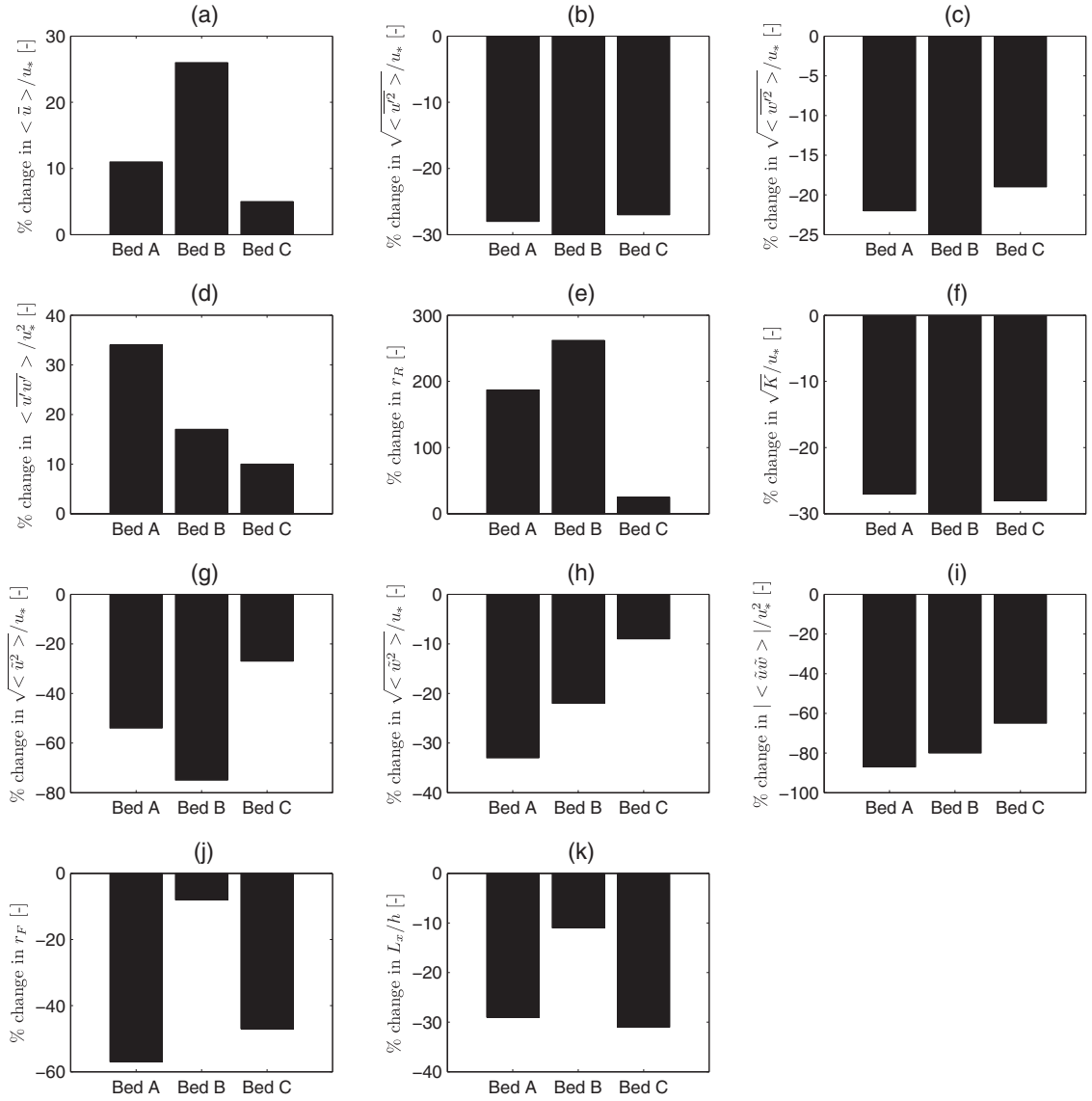

Figure 4. Percentage change in flow statistics at the roughness crest for the permeable bed relative to the impermeable bed.

turbulent kinetic energy is around 30% lower over the permeable beds (Table III; Figure 4(f)).

The spatial fluctuations in velocity are lower over the permeable beds (Figure 5(a), (b)). For example at the roughness crest the streamwise form-induced intensity is 27–77% lower (Figure 4(g)), and vertical form-induced intensity is 9–36% lower (Figure 4(h)). The momentum flux that arises from the correlations in these spatial fluctuations, in terms of the

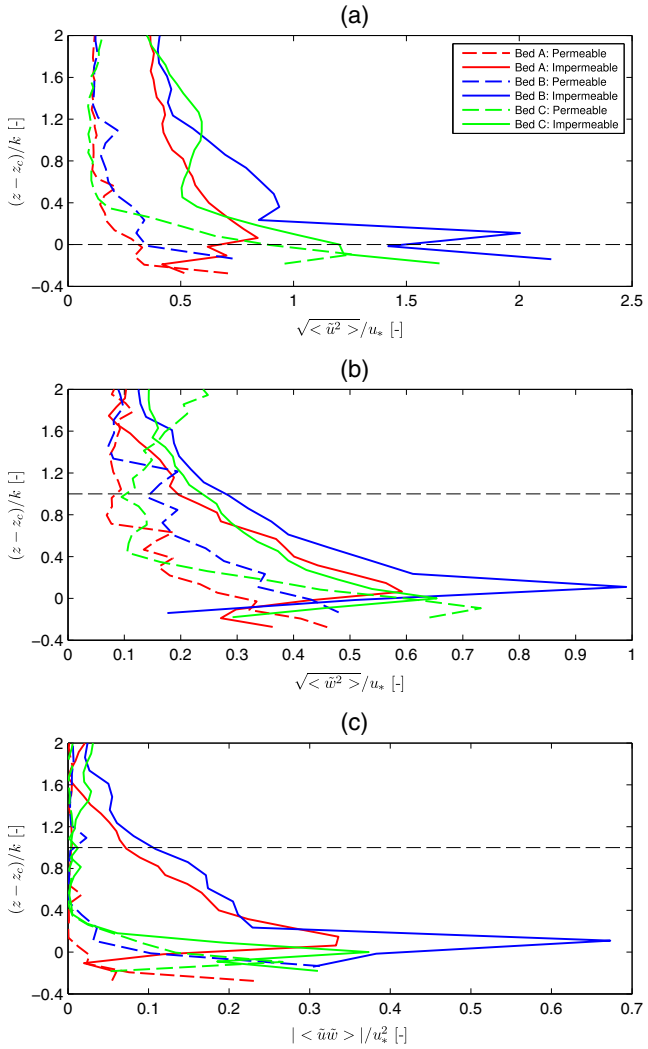

Figure 5. Vertical profiles of (a) streamwise form-induced intensity; (b) vertical form-induced intensity; and (c) absolute form-induced stress, where z is the measurement height, z_c is the roughness crest (= z_{99}) and k is the range of bed elevations. The dashed line denotes the top of the interfacial sublayer and the roughness crest. [Colour figure can be viewed at wileyonlinelibrary.com]

absolute form-induced stress, is also lower over the permeable beds (Figure 5(c), Table III). At the roughness crest, the stress is lower by a similar degree (87%, 82% and 65% lower over beds A, B and C; Figure 4(i)). These lower values occur because the form-induced stress correlation coefficient is smaller. For example, the coefficient is 0.2 for permeable Bed A and 0.5 for its impermeable equivalent (Table III). These lower coefficients reveal the spatial fluctuations are less correlated. Note that these two observations differ from those for the temporal fluctuations in velocity, and therefore form-induced stress makes a smaller contribution to overall momentum transfer, relative to the Reynolds stress, over the permeable beds.

Quadrant analysis

Table IV shows that at a hole size of zero the differences in the proportion of time spent in each quadrant are small. Ejection ($Q2$) and sweep ($Q4$) events dominate above each surface. At higher hole sizes, when low magnitude deviations from the mean are excluded, the differences become clear. First, the quadrant proportions reduce less quickly with an increase in hole size over the permeable bed. For example, at a hole size of zero the quadrant proportions are fairly similar between the permeable and impermeable beds (Table IV), but the slower decrease over the permeable bed results in the quadrant proportions at a hole size of one being more than double those over the impermeable bed (Figure 6). Second, at hole sizes of one and two, ejection and sweep events are more prevalent than inward- and outward-interactions over the permeable bed. For example over Bed A, ejection and sweeps are more than three times more prevalent than inward- and outward-interactions at hole sizes of one (Figure 6) and two over the permeable bed. However this dominance is not nearly as clear over the impermeable bed at these two hole sizes. This difference in ejection and sweep dominance helps explain the higher turbulence correlation coefficients observed over the permeable bed (Table III).

Spatial flow structure

Results from the two-point velocity correlation are shown in Figure 7. The figure displays contours of R_{uw} (x, 0, z) for Bed A, which is representative of the patterns observed for Beds B and C. The plot reveals a tilted, elliptical area of strong correlation ($R_{uw} > 0.2$) extending ~1.1 h in the streamwise direction and ~0.35 h in the vertical for the permeable bed (Figure 7(a)), and a slightly larger region of ~1.2 h and ~0.4 h for the impermeable bed (Figure 7(b)). The tilt angle of the major axis of the ellipse is ~25–30° relative to the bed. The elongation reflects the strongly anisotropic turbulence of longitudinal vortices commonly found in shear flows, and the tilt is characteristic of the sloping structures observed in gravel-bed flows (Roy *et al.*, 2004; Hardy *et al.*, 2009; Detert *et al.*, 2010a).

Table IV. Spatially-averaged proportion of time spent in each quadrant (%) $\langle T_{i,H} \rangle$, where i is the quadrant number and H is the hole size

	Bed A		Bed B		Bed C	
Parameter	**Permeable**	**Impermeable**	**Permeable**	**Impermeable**	**Permeable**	**Impermeable**
$\langle T_{1,0} \rangle$	19.5	15.5	19.5	22.7	19.8	22.3
$\langle T_{2,0} \rangle$	29.5	31.0	29.5	24.2	29.0	30.1
$\langle T_{3,0} \rangle$	21.5	24.8	22.4	20.5	23.4	15.0
$\langle T_{4,0} \rangle$	29.5	28.6	28.6	32.7	27.9	32.7
$\langle T_{1,1} \rangle$	3.3	1.2	3.6	1.5	3.7	1.0
$\langle T_{2,1} \rangle$	7.0	1.6	6.7	1.4	6.2	2.6
$\langle T_{3,1} \rangle$	2.9	1.4	3.0	1.3	3.1	1.1
$\langle T_{4,1} \rangle$	7.1	2.3	7.3	2.2	6.9	2.7
$\langle T_{1,2} \rangle$	1.1	0.6	1.2	0.9	1.2	0.7
$\langle T_{2,2} \rangle$	2.5	0.8	2.5	0.9	2.2	1.2
$\langle T_{3,2} \rangle$	0.8	0.9	0.9	0.6	0.8	0.7
$\langle T_{4,2} \rangle$	2.6	0.8	2.7	0.9	2.6	1.1

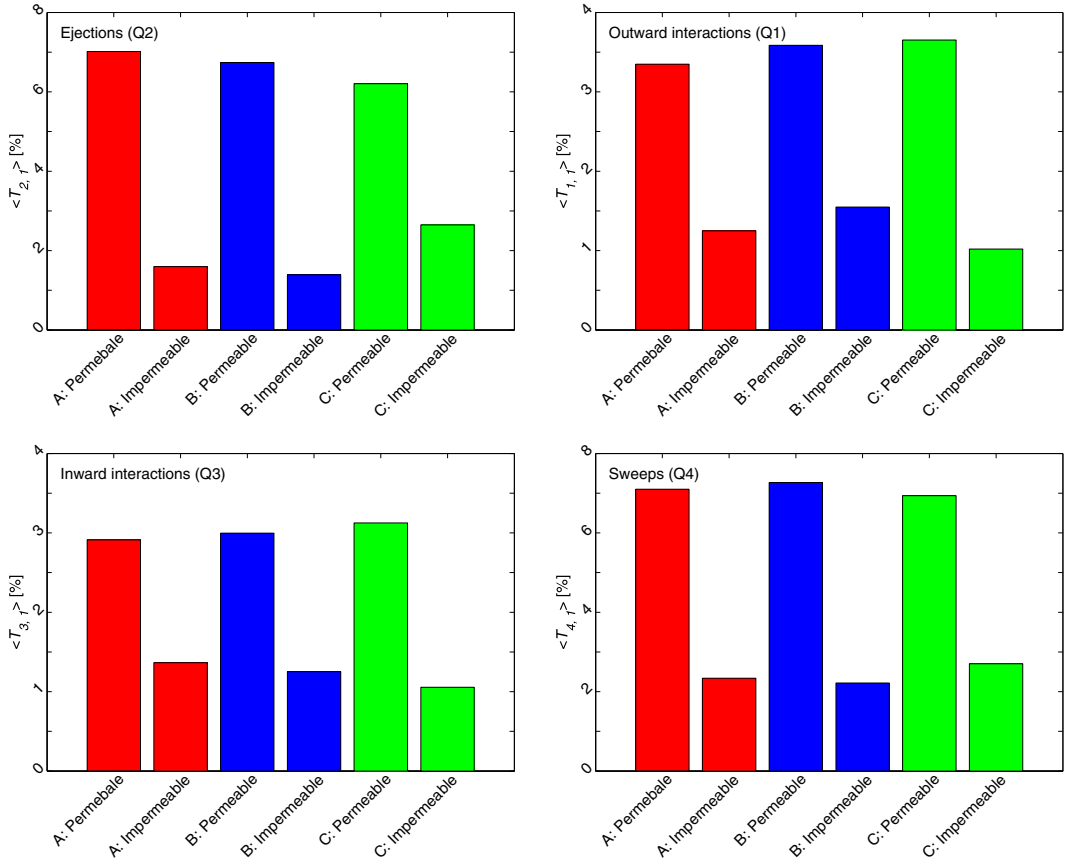

Figure 6. Spatial coverage of the four quadrants at a hole size of one. [Colour figure can be viewed at wileyonlinelibrary.com]

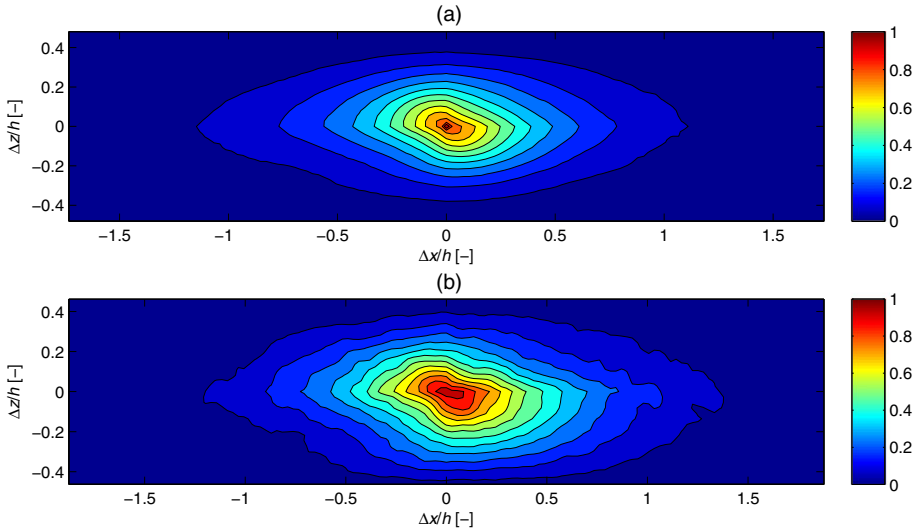

Figure 7. Change in the two-point correlation coefficient between u' and w' in the streamwise and vertical directions for (a) permeable Bed A and (b) its impermeable facsimile. [Colour figure can be viewed at wileyonlinelibrary.com]

The concentrated region of strong correlation around $\Delta x = 0$, $\Delta z = 0$ is smaller over the permeable bed, and is reflected in the smaller streamwise length scales (Table III; Figure 4(k)). The shorter eddy lengths cannot be explained by a slower mean flow velocity given the mean flow velocity was consistently higher over the permeable bed, and must therefore reflect a differing spatial flow organisation. The difference in vertical length scales is less than the spatial resolution of the PIV measurements (Table III), and thus can be considered similar for permeable and impermeable beds.

Figure 8 shows the distribution of the kinetic energy associated with the first 10 POD-modes. The distributions reveal that a higher proportion of energy is contained within these modes over the permeable beds. Of particular significance for understanding the relative importance of coherent eddies in producing TKE is the much higher proportion of energy associated with the first three modes. Taking Bed B as an example, 27% of energy is contained within these modes over the permeable bed but is just 9% over the impermeable bed. To put this in perspective, if all the vector fields were completely random and uncorrelated, then all modes would represent approximately ~0.1% each of the total energy. The results reveal that a higher fraction of kinetic energy is caused by coherent motions over the permeable than the impermeable beds,

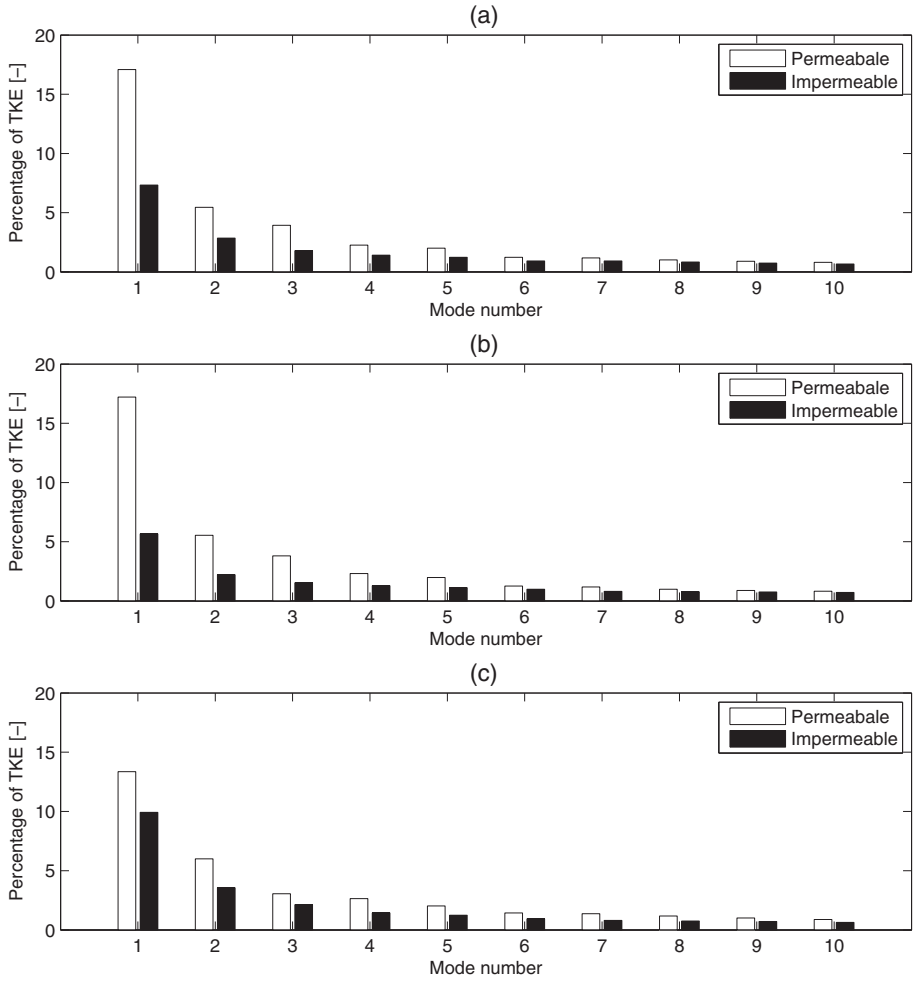

Figure 8. Distribution of the kinetic energy associated with POD-modes for (a) Bed A, (b) Bed B and (c) Bed C. The first 10 modes are shown because less than 1% of energy is contained in a mode greater than 10.

further explaining why the Reynolds stress, and its correlation coefficient, is higher.

Discussion

Effect of bed permeability on near-bed hydrodynamics

The differences in near-bed hydrodynamics between the permeable and impermeable beds are summarised in Table V. The key inferences from these differences are as follows. First, the larger turbulence correlation coefficients over the permeable bed suggest that the turbulence is in some sense more organised. The quadrant and POD analysis would suggest this greater organisation is because the eddies are more coherent. Combined with the lower turbulence intensities, higher Reynolds stress and a higher fraction of kinetic energy caused by coherent motions, these observations indicate that turbulence over the permeable bed transports substantially more momentum per unit of velocity variance. Thus turbulence is more efficient at momentum transfer. This higher efficiency occurs because: (i) the flow can penetrate into the subsurface and interact with the pore water, unlike the impermeable bed in which a no-slip condition applies at the solid surface; and (ii) more high stress producing ejections and sweeps over the permeable bed enhance the mixing of high and low velocity fluid and therefore the drawing down of momentum towards the bed.

Table V. Summary of the differences in near-bed hydrodynamics between permeable and impermeable beds

Parameter	Permeable bed is...
Double-averaged velocity	Higher
Turbulence intensity	Lower
Reynolds stress	Higher
Turbulence correlation coefficient	Higher
Turbulent kinetic energy	Lower
Prevalence of high stress producing ejections and sweeps	Higher
Fraction of turbulent kinetic energy caused by coherent motions	Higher
Eddy length	Lower
Eddy height	Similar
Spatial fluctuations in velocity	Lower
Form-induced stress	Lower
Form-induced momentum flux	Lower

Second, this higher efficiency and a lower turbulent kinetic energy (indicating less energy is extracted from the mean flow by turbulence) is the probable reason for the higher double-averaged velocity, and therefore lower bulk flow resistance over the permeable bed. This explanation has traction when it is considered that hydrodynamically-driven, shallow hyporheic flows that occur through pathways that are typically the size of gravel pore spaces (Nagaoka and Ohgaki, 1990; Käser *et al.*, 2013) scale positively with mean stream velocity (Elliott and Brooks, 1997; Packman *et al.*, 2000; Salehin *et al.*, 2004).

Third, momentum transfer not only differs between the two beds in terms of efficiency but also in the manner in which momentum is transferred. Over the permeable bed a smaller proportion of momentum is transferred from the overlying flow to the surface grains by form-induced stress (caused by persistent vortices behind these grains) and a greater proportion is transferred by Reynolds stress caused by turbulent fluctuations in the flow. Grain-scale interfacial transport is usually induced by turbulent coupling between the overlying and pore water flow (Packman and Bencala, 2000; Huettel and Webster, 2001; Boano *et al.*, 2014). Therefore this greater turbulent fluid exchange is consistent with observations of faster hydrodynamically-driven, shallow hyporheic exchange in more permeable river beds (Packman *et al.*, 2004).

Fourth, the quadrant and POD analysis revealed that coherent motions, particularly sweeps and ejections, are more prevalent temporally and play a more critical role in the production of TKE over permeable beds. This difference in coherent motion is probably for the following reason. Below an impermeable bed there is no subsurface flow to promote the production of intense ejections transferring fluid from the pores of the bed to the overlying flow, and when a sweep coming from above interacts with a solid surface its vertical motions are impeded and the energy is transferred downwards with almost zero vertical velocity. This scenario is in contrast to a permeable bed where a sweep can move into the pore space, have a non-zero vertical velocity and produce zones of high momentum downwelling above the bed surface (Blois *et al.*, 2014). Also, ejections are more likely to occur because low momentum fluid can be transferred from the subsurface to the overlying flow, producing upwelling and horseshoe-shaped vortices just above the bed surface (Sinha *et al.*, 2017). Thus a higher turbulence correlation coefficient, higher Reynolds stress, and a greater contribution of turbulence to momentum transfer are observed over the permeable bed. The observed difference in the coherent motions makes sense when you consider the results of flume experiments by Nagaoka and Ohgaki (1990) and numerical simulations by Boano *et al.* (2011), who both showed that these motions are critical for the pumping of water in and out of the bed. More specifically these studies revealed two important results: (i) small turbulent eddies, whose maximum size is similar to the grain size, cause fast and efficient water exchange with shallow sediment layers. This aligns with the higher prevalence of high stress producing ejections and sweeps we observed over the permeable beds, driving sediment–water exchange through the ejection of more low-momentum fluid away from the bed and sweeping more high-momentum fluid toward the bed. These downward and upward motions produce high and low pressure zones that cause 'blowing' and 'suction' of water at the sediment–water interface, inducing the pumping of water in and out of the bed; and (ii) large flow structures play a dominant role in the pumping of water deep into the bed subsurface, suggesting that large eddies make a greater contribution to turbulent momentum transfer at the sediment–water interface of permeable beds. This aligns with our observation that large eddies played a greater role in the production of turbulent kinetic energy.

Implications

A number of important implications for river flows emerge from our results. First, the local pressure gradients across the sediment–water interface are likely to differ between impermeable and permeable beds, particularly in terms of the balance between the steady and fluctuating component of these gradients. Our results revealed that spatial fluctuations in velocity are lower and less coherent over a permeable bed, and therefore the steady, time-averaged bed pressure distribution is likely to be narrower. In contrast the more coherent turbulent flow is likely to lead to higher fluctuating pressures (Boano *et al.*, 2011; Detert *et al.*, 2010a). Given material transport is driven by these local pressure gradients, the rates of dissolved, bedload and suspended material transport across the sediment–water interface will differ between permeable and impermeable beds. Thus the effect of bed permeability on near-bed hydrodynamics is likely to have a critical impact on benthic habitat availability.

Second, hydraulic (Keylock *et al.*, 2012) and hyporheic flow models that simulate the velocity and bed pressure distribution over an impermeable bed (Cardenas and Wilson, 2007; Qian *et al.*, 2008; Zhou *et al.*, 2014), may yield unrealistic predictions of the turbulence and spatial characteristics of near-bed hydraulics, and flow through the bed. By isolating differences in surface topography using facsimiles, our results demonstrate that the differences in hydrodynamics over permeable and impermeable bed must be due to the exchange of flow between the overlying flow and subsurface. More realistic flow models should thus include surface–subsurface flow interactions and their affect on the overlying flow dynamics and resulting local pressure gradients.

Third, more sophisticated flow resistance models are required for coarse-grained rivers. The common approach is to estimate resistance parameters, such as the Manning coefficient or equivalent sand roughness height, from the measurement of a characteristic grain diameter (Hey, 1979; Bray, 1985; Wiberg and Smith, 1991) or the standard deviation in bed elevations (Aberle and Smart, 2003; Coleman *et al.*, 2011). By using such an approach, the same flow resistance for permeable and impermeable beds would be predicted. We show that this is an inappropriate procedure because a permeable bed has lower flow resistance than an impermeable bed. Therefore flow resistance should be predicted by examining not only the bed surface but also the bed's permeability.

Bed material size and the size, spacing and sequencing of bedforms all affect sediment–water exchange (Nagaoka and Ohgaki, 1990; Elliott and Brooks, 1997; Boano *et al.*, 2014). Clearly future work needs to investigate further the effect of bed permeability over a wider range of water-worked bed conditions, and examine the links between bed porosity geometry and sediment–water fluid exchange processes. In addition there is a need to observe surface–subsurface flow coupling and to extend the study over different flow conditions, given that subsurface flow is contingent upon the Reynolds and Froude numbers (Blois *et al.*, 2012), mean flow velocity (Elliott and Brooks, 1997; Packman *et al.*, 2000; Salehin *et al.*, 2004), and relative submergence (Tonina and Buffington, 2007). For example, one might expect the differences in hydrodynamics between permeable and impermeable beds to be greater at higher Reynolds number and mean flow velocities because pore water velocity and turbulence correlate positively with these flow parameters (Elliott and Brooks, 1997; Packman *et al.*, 2000; Salehin *et al.*, 2004; Blois *et al.*, 2012).

Conclusions

Novel laboratory experiments in a recirculating flume have quantified, for the first time, how the permeability of water-worked gravel beds affect hydrodynamics close to the bed. Turbulent eddies remain more coherent over permeable beds and this is evident in less intense, more organised turbulence and more efficient momentum transfer. Furthermore, turbulent kinetic energy is lower, indicating that less energy is extracted from the mean flow by this turbulence. Consequently, the

double-averaged velocity is higher and the bulk flow resistance is lower over permeable beds. The manner in which momentum is transferred from the overlying flow to the surface grains is also different, with higher Reynolds stress but lower form-induced stress over permeable beds. These results indicate that there are fundamental differences in the near-bed flows over permeable and impermeable beds. There are three main implications. First, the local pressure gradients, and therefore the rates of dissolved, bedload and suspended material transport across the sediment–water interface will differ between impermeable and permeable beds. Second, near-bed and hyporheic flows are unlikely to be adequately predicted by numerical models that represent the bed as an impermeable boundary. Third, more sophisticated flow resistance models are required for coarse-grained rivers that consider not only the bed surface but also the underlying permeable structure. Together, these three observations suggest that improved numerical modelling of river hydrodynamics, hyporheic flow and material transport require incorporation of subsurface–surface flow feedbacks that are currently absent.

More generally, our results demonstrate that bed permeability is an important control on aspects of near-bed hydrodynamics that influence hyporheic exchange, fluvial sediment dynamics and benthic habitat availability. In this case, understanding more about surface–subsurface flow coupling represents an important research frontier for river scientists.

Acknowledgements—This project was supported financially by the Natural Environment Research Council of the UK through NE/H020772/1 (awarded to Powell) and NE/H020993/1 (awarded to Rice). We are grateful to Judy Haschenburger, John Pitlick and Tom Lisle for sharing particle size distributions from gravel bed rivers in New Zealand and the USA. We thank the Associate Editor and reviewers for their helpful comments and suggestions.

References

Aberle J, Smart GM. 2003. The influence of roughness structure on flow resistance on steep slopes. *Journal of Hydraulic Research* **41**: 259–269.

Bathurst JC. 1985. Theoretical aspects of flow resistance. *Gravel-bed Rivers*. In Hey RD, Bathurst JC, Thorne CR (eds). John Wiley & Sons: Chichester; 83–108.

Bathurst JC. 1993. Flow resistance through the channel network. In *Channel Network Hydrology*, Bevan K, Kirkby MJ (eds). John Wiley and Sons: Chichester; 69–98.

Battin TJ, Kaplan LA, Findlay S, Hopkinson CS, Marti E, Packman AI, Newbold JD, Sabater F. 2008. Biophysical controls on organic carbon fluxes in fluvial networks. *Nature Geoscience* **1**: 95–100.

Bencala KE, Gooseff MN, Kimball BA. 2011. Rethinking hyporheic flow and transient storage to advance understanding of stream-catchment connections. *Water Resources Research* **47**. https://doi.org/10.1029/2010wr010066.

Bertin S, Friedrich H. 2014. Measurement of gravel-bed topography: evaluation study applying statistical roughness analysis. *Journal of Hydraulic Engineering, ASCE* **140**: 269–279.

Blois G, Sambrook Smith GH, Best JL, Hardy RJ, Lead JR. 2012. Quantifying the dynamics of flow within a permeable bed using time-resolved endoscopic particle imaging velocimetry (EPIV). *Experiments in Fluids* **53**: 51–76. https://doi.org/10.1007/s00348-011-1198-8.

Blois G, Best JL, Sambrook Smith GHS, Hardy RJ. 2014. Effect of bed permeability and hyporheic flow on turbulent flow over bed forms. *Geophysical Research Letters* **41**: 6435–6442.

Boano F, Revelli R, Ridolfi L. 2011. Water and solute exchange through flat streambeds induced by large turbulent eddies. *Journal of Hydrology* **402**: 290–296.

Boano F, Harvey JW, Marion A, Packman AI, Revelli R, Ridolfi L, Wörman A. 2014. Hyporheic flow and transport processes: mechanisms, models, and biogeochemical implications. *Reviews of Geophysics* **52**: 603–679.

Boulton AJ, Findlay S, Marmonier P, Stanley EH, Valett HM. 1998. The functional significance of the hyporheic zone in streams and rivers. *Annual Review of Ecology and Systematics* **29**: 59–81.

Bray DI. 1985. Flow resistance in gravel-bed rivers. In *Gravel-bed Rivers*, Hey RD, Bathurst JC, Thorne CR (eds). John Wiley & Sons: Chichester; 109–132.

Buffin-Bélanger T, Reid I, Rice S, Chandler JH, Lancaster J. 2003. A casting procedure for reproducing coarse-grained sedimentary surfaces. *Earth Surface Processes and Landforms* **28**: 787–796.

Buffin-Bélanger T, Roy AG. 2005. 1 min in the life of a river: selecting the optimal record length for the measurement of turbulence in fluvial boundary layers. *Geomorphology* **68**: 77–94.

Cardenas MB, Wilson JL. 2007. Effects of current-bed form induced fluid flow on the thermal regime of sediments. *Water Resources Research* **43**. https://doi.org/10.1029/2006wr005343.

Chen C, Packman AI, Zhang D, Gaillard J-F. 2010. A multi-scale investigation of interfacial transport, pore fluid flow, and fine particle deposition in a sediment bed. *Water Resources Research* **46**. https://doi.org/10.1029/2009wr009018.

Coleman SE, Nikora VI, Aberle J. 2011. Interpretation of alluvial beds through bed-elevation distribution moments. *Water Resources Research* **47**. https://doi.org/10.1029/2011wr010672.

Cooper JR, Aberle J, Koll K, Tait SJ. 2013. Influence of relative submergence on spatial variance and form-induced stress of gravel-bed flows. *Water Resources Research* **49**: 5765–5777. https://doi.org/10.1002/wrcr.20464.

Cooper JR, Tait SJ. 2009. Water-worked gravel beds in laboratory flumes - a natural analogue? *Earth Surface Processes and Landforms* **34**: 384–397.

Cooper JR, Tait SJ. 2010. Examining the physical components of boundary shear stress for water-worked gravel deposits. *Earth Surface Processes and Landforms* **35**: 1240–1246.

Detert M, Jirka GH, Jehle M, Klar M, Jähne B, Köhler H-J, Wenka T. 2004. Pressure fluctuations within subsurface gravel bed caused by turbulent open-channel flow. In *River Flow 2004: Proceedings of the Second International Conference on Fluvial Hydraulics*, 23–25 June 2004, Napoli, Italy, Greco M, Carravetta A, Della Morte R (eds), Vol. **1**. Taylor and Francis: London.

Detert M, Nikora V, Jirka G. 2010a. Synoptic velocity and pressure fields at the water–sediment interface of streambeds. *Journal of Fluid Mechanics* **660**: 55–86. https://doi.org/10.1017/S0022112010002545.

Detert M, Weitbrecht V, Jirka GH. 2010b. Laboratory measurements on turbulent pressure fluctuations in and above gravel beds. *Journal of Hydraulic Engineering, ASCE* **136**: 779–789.

Elliott AH, Brooks NH. 1997. Transfer of nonsorbing solutes to a streambed with bed forms: theory. *Water Resources Research* **33**: 123–136.

Finnigan JJ, Shaw RH. 2008. Double-averaging methodology and its application to turbulent flow in and above vegetation canopies. *Acta Geophysica* **56**: 534–561.

Folk RL, Ward WC. 1957. Brazos river bar: a study of the significance of grain size parameters. *Journal of Sedimentary Petrology* **27**: 3–26.

Fukunaga K. 1990. *Introduction to Statistical Pattern Recognition*. Academic Press: San Diego; CA.

Hardy RJ, Best JL, Lane SN, Carbonneau PE. 2009. Coherent flow structures in a depth-limited flow over a gravel surface: the role of near-bed turbulence and influence of Reynolds number. *Journal of Geophysical Research* **114**. https://doi.org/10.1029/2007JF000970.

Harvey JW, Bencala KE. 1993. The effect of streambed topography on surface-subsurface water exchange in mountain catchments. *Water Resources Research* **29**: 89–98.

Haynes H, Ockelford A-M, Vignaga E, Holmes WM. 2012. A new approach to define surface/sub-surface transition in gravel beds. *Acta Geophysica* **60**: 1589–1606 15https://doi.org/10.2478/s11600-11012-10067-z.

Hey RD. 1979. Flow resistance in gravel-bed rivers. *Journal of the Hydraulics Division ASCE* **105**: 365–379.

Hodge R, Brasington J, Richards K. 2009. Analysing laser-scanned digital terrain models of gravel bed surfaces: linking morphology to sediment transport processes and hydraulics. *Sedimentology* **56**: 2024–2043.

Huettel M, Webster IT. 2001. Porewater flow in permeable sediments. In *The Benthic Boundary Layey Tonina and Buffington,* (*2009*),

Boudreau BP, Jørgensen BB (eds). Oxford University Press: Oxford; 144–179.

Käser DH, Binley A, Heathwaite AL. 2013. On the importance of considering channel microforms in groundwater models of hyporheic exchange. *River Research and Applications* **29**: 528–535.

Keylock CJ, Constantinescu G, Hardy RJ. 2012. The application of computational fluid dynamics to natural river channels: eddy resolving versus mean flow approaches. *Geomorphology* **179**: 1–20.

Lu SS, Willmarth W. 1973. Measurements of structure of Reynolds stress in a turbulent boundary-layer. *Journal of Fluid Mechanics* **60**: 481–511.

Marion A, Packman AI, Zaramella M, Bottacin-Busolin A. 2008. Hyporheic flows in stratified beds. *Water Resources Research* **44**. https://doi.org/10.1029/2007wr006079.

Marion A, Tait SJ, McEwan IK. 2003. Analysis of small-scale gravel bed topography during armoring. *Water Resources Research* **39**. https://doi.org/10.1029/2003wr002367.

Mignot E, Barthelemy E, Hurther D. 2009. Double-averaging analysis and local flow characterization of near-bed turbulence in gravel-bed channel flows. *Journal of Fluid Mechanics* **618**: 279–303.

Moin P, Moser RD. 1989. Characteristic-eddy decomposition of turbulence in a channel. *Journal of Fluid Mechanics* **200**: 471–509.

Mulholland PJ, Helton AM, Poole GC, Hall RO, Jr, Hamilton SK, Peterson BJ, Tank JL, Ashkenas LR, Cooper LW, Dahm CN, Dodds WK, Findlay SEG, Gregory SV, Grimm NB, Johnson SL, McDowell WH, Meyer JL, Valett HM, Webster JR, Arango CP, Beaulieu JJ, Bernot MJ, Burgin AJ, Crenshaw CL, Johnson LT, Niederlehner BR, O'Brien JM, Potter JD, Sheibley RW, Sobota DJ, Thomas SM. 2008. Stream denitrification across biomes and its response to anthropogenic nitrate loading. *Nature* **452**: 202–U246.

Nagaoka H, Ohgaki S. 1990. Mass transfer mechanism in a porous riverbed. *Water Research* **24**: 417–426.

Nikora V, McEwan I, McLean S, Coleman S, Pokrajac D, Walters R. 2007. Double-averaging concept for rough-bed open-channel and overland flows: Theoretical background. *Journal of Hydraulic Engineering, ASCE* **133**: 873–883.

Packman A, Salehin M, Zaramella M. 2004. Hyporheic exchange with gravel beds: Basic hydrodynamic interactions and bedform-induced advective flows. *Journal of Hydraulic Engineering, ASCE* **130**: 647–656.

Packman AI, Bencala KE. 2000. Modeling surface-subsurface hydrological interactions. In *Streams and Ground Waters*, Jones JB, Mulholl PJ (eds). Academic Press: San Diego, CA; 45–80.

Packman AI, Brooks NH, Morgan JJ. 2000. A physicochemical model for colloid exchange between a stream and a sand streambed with bed forms. *Water Resources Research* **36**: 2351–2361.

Palumbo-Roe B, Wragg J, Banks VJ. 2012. Lead mobilisation in the hyporheic zone and river bank sediments of a contaminated stream: contribution to diffuse pollution. *Journal of Soils and Sediments* **12**: 1633–1640.

Qian Q, Voller VR, Stefan HG. 2008. A vertical dispersion model for solute exchange induced by underflow and periodic hyporheic flow in a stream gravel bed. *Water Resources Research* **44**. https://doi.org/10.1029/2007wr006366.

Roy AG, Buffin-Bélanger T, Lamarre H, Kirkbride AD. 2004. Size, shape and dynamics of large-scale turbulent flow structures in a gravel-bed river. *Journal of Fluid Mechanics* **500**: 1–27.

Salehin M, Packman AI, Paradis M. 2004. Hyporheic exchange with heterogeneous streambeds: Laboratory experiments and modeling. *Water Resources Research* **40**. https://doi.org/10.1029/2003wr002567.

Sawyer AH, Cardenas MB. 2009. Hyporheic flow and residence time distributions in heterogeneous cross-bedded sediment. *Water Resources Research* **45**. https://doi.org/10.1029/2008wr007632.

Shaw RH, Brunet Y, Finnigan JJ, Raupach MR. 1995. A wind tunnel study of air flow in waving wheat: Two-point velocity statistics. *Boundary-Layer Meteorology* **76**: 349–376.

Sinha S, Hardy RJ, Blois G, Best JL, Smith GHS. 2017. A numerical investigation into the importance of bed permeability on determining flow structures over river dunes. *Water Resources Research* **53**: 3067–3086. https://doi.org/10.1002/2016wr019662.

Suttle KB, Power ME, Levine JM, McNeely C. 2004. How fine sediment in riverbeds impairs growth and survival of juvenile salmonids. *Ecological Applications* **14**: 969–974.

Tonina D, Buffington JM. 2007. Hyporheic exchange in gravel bed rivers with pool-riffle morphology: Laboratory experiments and three-dimensional modeling. *Water Resources Research* **43**: https://doi.org/W01421. https://doi.org/10.1029/2005WR004328.

Wiberg PL, Smith JD. 1991. Velocity distribution and bed roughness in high-gradient streams. *Water Resources Research* **27**: 825–838.

Williams GP. 1970. Flume width and water depth effects in sediment transport experiments. *Professional Paper 562-H*, USA Geological Survey, Washington, USA.

Zhou Y, Ritzi RW, Jr, Soltanian MR, Dominic DF. 2014. The influence of streambed heterogeneity on hyporheic flow in gravelly rivers. *Groundwater* **52**: 206–216.